



UTRECHT UNIVERSITY

Chiral plasmonic nanohelices

Author:
N.D.Kosters B.Sc.

Supervisors:
A. de Hoogh M.Sc.
Prof. Dr. L. Kuipers
Dr. D. van Oosten



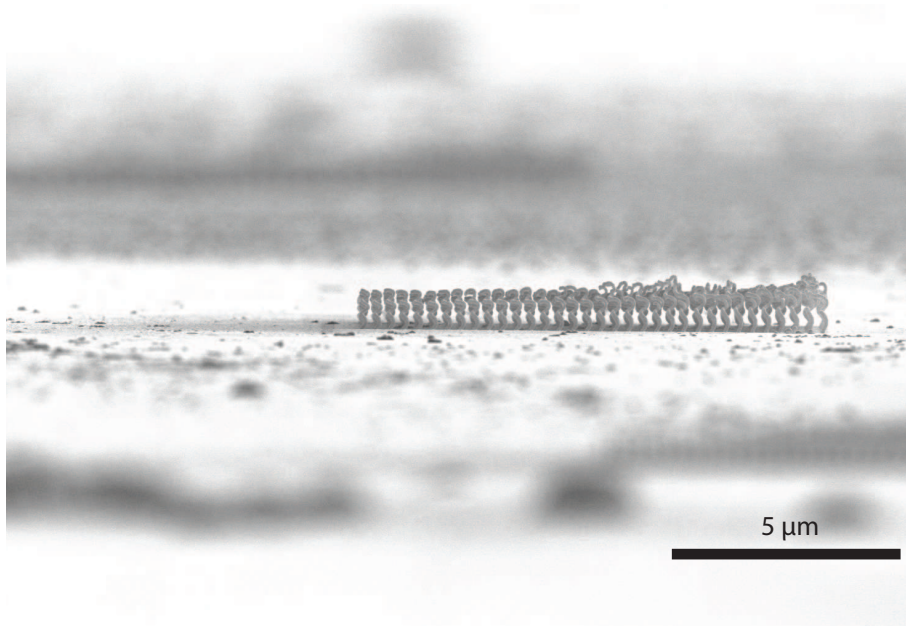
FOM INSTITUTE AMOLF, AMSTERDAM
NANOOPTICS GROUP

August 13, 2014

Abstract

Chirality of three-dimensional structures, i.e. structures that cannot be superimposed on their mirror image, is a very common geometric property in nature. Chirality has generated a lot of excitement in recent years, as man-made chiral metamaterials have, for example, greatly improved biosensors [1]. Fabrication of such complex three-dimensional nanostructures is a challenging process, particularly for visible light applications, where the corresponding structure sizes are on the nanoscale. Here, we show how electron beam induced deposition can be used to fabricate periodic arrays of core-shell (fused silica - gold) nanohelices. We detail the fabrication process used to create these nanoscopic, chiral plasmonic structures, focusing on the procedure that allows us to create arrays of identical helices.

Transmission measurements on the chiral plasmonic nanohelices are used to differentiate between the way in which right- and left-circularly polarized light interact with these structures, an effect called optical activity. We measure the optical activity of arrays of plasmonic nanohelices and determine how the optical activity is influenced by different helix heights. Experimental results are compared with calculations for better understanding.



An array of nanohelices.

Contents

1	Introduction	1
1.1	Nanoplasmonics	1
1.2	Chirality	1
1.3	Circular polarization and optical activity	3
1.4	Thesis outline	5
2	Fabrication of nanohelices	6
2.1	Electron beam induced deposition and sputtercoating	7
2.2	Delicate interplay between factors	15
3	Optical measurements	17
3.1	Sample characterization	17
3.2	Experimental setup	19
3.3	Results	20
4	Numerical calculations	24
4.1	Model description	24
4.2	Results	26
5	Discussion and Outlook	29
5.1	Comparison experiment with calculations	29
5.2	Outlook	30
6	Acknowledgements	34
	Appendix A Structure of a streamfile	35

1 Introduction

1.1 Nanoplasmonics

Nanotechnology is a hot topic. In many scientific fields and in industry but also in daily language, where it used to be ‘micro’, now ‘nano’ is the prefix that is very willingly used as a synonym of ‘small’. The fabrication and use of materials at the nanoscale, a trend of miniaturization which finds its roots in the electronics industry, is widely called nanotechnology. For instance in solar cell research, nanotechnology is very promising in increasing the efficiency of solar cells. Nanostructures can manipulate light at the nanoscale in such a way that light absorption in the cell is enhanced [2, 3]. When nanostructures are metallic, the field of nanoplasmonics is entered, which studies the optical phenomena on the nanoscale in metal nanostructures [4].

When a metal nanoparticle in a dielectric medium is illuminated by an electromagnetic wave, the free electrons in the metal nanoparticle move as a response to the electric field of the electromagnetic wave. In this E-field, the (negative) electrons in the particle shift with respect to the (positive) lattice ions and immediately, since opposite charges attract, a restoring force exists, opposite to the E-field, leading to an oscillation of the free electrons. These free-electron oscillations at a metal-dielectric interface, of for instance the metal nanoparticle in a dielectric medium, are known as surface plasmons, localized modes that confine optical energy to an interface. When coupling occurs between the free-electron oscillations and electromagnetic fields in the metal and dielectric, these modes can propagate along the metal-dielectric interface and these traveling modes are known as surface plasmon polaritons [5]. Studies in the field of nanoplasmonics have led to interesting discoveries as for example super-efficient transmission of light through subwavelength metallic holes [6].

1.2 Chirality

Chirality of three-dimensional structures is a very common geometric property in nature. Objects of opposite chirality, enantiomers, are each others mirror image and have many identical physical properties as for example density, volume and electrical conductivity. The most prominent example of a chiral object is the human hand. A left- and right-hand are each others mirror image but no physical translation or rotation will turn a left-hand into a right-hand, which is the definition of a chiral geometry. Since the human hand is such an illustrative example of a chiral geometry, the term right- or left-handed is commonly used to describe the two enantiomers. An enantiomer then is defined as either ‘left-handed’ or ‘right-handed’.

In Figure 1.1 the chiral geometry of a helix is shown. The two helices displayed are each others exact mirror image but the two enantiomers cannot be superimposed on each other. The helix on the left is a right-handed helix because it makes a right-handed twist. Likewise, the other helix is called left-handed since it makes a left-handed twist.

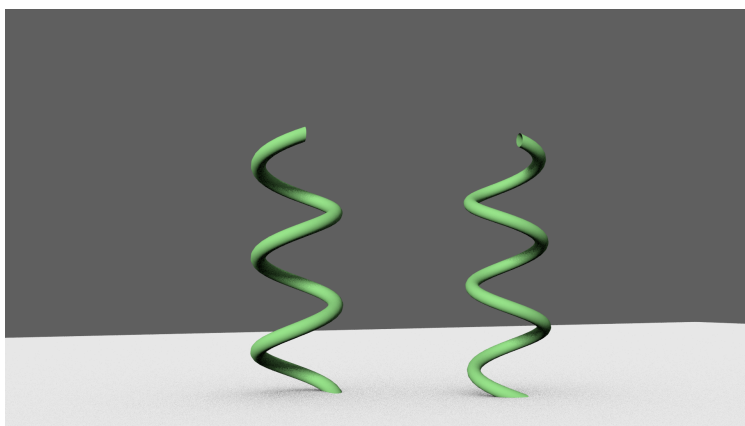


Figure 1.1: Opposite enantiomers of a helix. The enantiomers are each others mirror image. No translation or rotation can change the left enantiomer into the right enantiomer. In this case, the helix on the left is right-handed, as it makes a twist to the right. The helix on the right is left-handed, as it makes a twist to the left. Note that this twist is the same seen from the bottom and from the top.

Chirality has generated a lot of excitement in recent years due to the fundamental presence of it in nature [7]. Starting with molecules, amino acids, the building blocks of proteins that are present in all living cells, are chiral. Amino acids primarily exist as the left-handed enantiomer of the molecule and the corresponding biological processes in which these left-handed molecules are involved are stereo selective; the processes only can occur with the left-handed enantiomer and not with the right-handed enantiomer. Amino acids also form the well known nucleic acid DNA. DNA is remarkable since it is built up by chiral molecules but also has a chiral geometry itself: the double helix geometry. Furthermore enzymes, nature's catalysts, can be sensitive to chirality and only produce or bind to one of two enantiomers of molecules.

Excitement arose when a probing technique was developed to distinguish the enantiomers of chiral molecules. In the pharmaceutical industry, distinction between two enantiomers is of great importance for drug development. The effect of one enantiomer of a molecule in a drug can be very different from the effect of the other enantiomer [8]. This probing technique is based on different interactions of molecules with left-handed circularly polarized light (LCP) compared to right-handed circularly polarized light (RCP). This difference is referred to as 'optical activity'.

1.3 Circular polarization and optical activity

Polarization of a wave can be transversal. A transverse polarized wave has a displacement from equilibrium perpendicular to the direction of propagation. An electromagnetic wave is a physical example of a transverse wave. In case of an electromagnetic plane wave, the electric field vector represents the direction and amplitude the electric field. If the propagation of the plane wave is, for example, in the \hat{z} -direction, the electric field vector can point somewhere in the \hat{x} - \hat{y} plane and can be defined as [9]

$$\mathbf{E}(z, t) = \text{Re}(\mathbf{A}e^{i(\omega t - kz)}) \quad (1.1)$$

where $\mathbf{E}(z, t)$ is the electric field vector and \mathbf{A} is a complex vector in the \hat{x} - \hat{y} plane described by

$$\mathbf{A} = \hat{\mathbf{x}}A_x e^{i\delta_x} + \hat{\mathbf{y}}A_y e^{i\delta_y}. \quad (1.2)$$

After some steps of algebra [9], the trace of the point of the electric field vector \mathbf{E} in time and space can be described by the coordinates (E_x, E_y) following

$$\begin{aligned} E_x &= A_x \cos(\omega t - kz) \\ E_y &= A_y \cos(\omega t - kz + \delta) \end{aligned} \quad (1.3)$$

where $\delta = \delta_y - \delta_x$. The phase angle δ is defined in the range $-\pi < \delta \leq \pi$. When this phase angle is such that the point of the electric field vector describes a circle in space in time, the plane wave is called to be circularly polarized. This is the case for $\delta = -\pi/2$ and $\delta = \pi/2$. In Figure 1.2 the resulting trace of the tip of the electric field vector is displayed for $A_x = A_y$ and $\delta = \pm\pi/2$. Right-handed circularly polarized light is displayed in Figure 1.2a when $\delta = -\pi/2$ and left-handed circularly polarized light is displayed in Figure 1.2b when $\delta = \pi/2$. These polarizations correspond to the point of view of the source ('S' in Figure 1.2), note that it looks different for the receiver ('R' in Figure 1.2). The trace of the point of the electric field vector evolving in time looks helical, comparable to the helices in Figure 1.1.

The optical activity of a material is determined by comparing transmission of left-handed circularly polarized light (LCP) with that of right-handed circularly polarized light (RCP) through the material following

$$\text{optical activity (O.A.)} = \frac{T_{\text{LCP}} - T_{\text{RCP}}}{T_{\text{RCP}} + T_{\text{LCP}}} \quad (1.4)$$

where T_{LCP} stands for the transmission coefficient of LCP. An arbitrary choice can be made in subtracting $T_{\text{LCP}} - T_{\text{RCP}}$ or $T_{\text{RCP}} - T_{\text{LCP}}$.

Now imagine combining the field of nanoplasmonics with chirality by making chiral plasmonic nanostructures. Plasmonics induce strong optical interaction [4] and optical phenomena as optical activity are possibly increased. Therefore, in recent years, many chiral plasmonic nanostructures have been fabricated [10–13]. Applications using these specific chiral plasmonic nanostructures have also been demonstrated. For

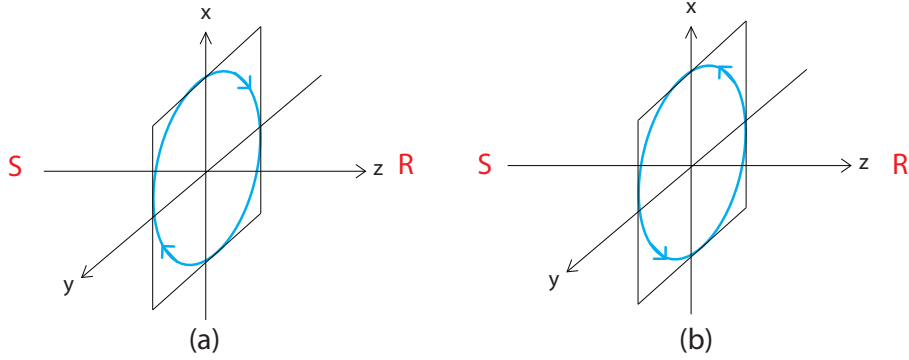


Figure 1.2: Schematic representation of circular polarization as defined in this thesis. Blue represents the trace of the point of the electric field vector \mathbf{E} . A helical trace is formed while propagating in the z -direction in time. (a) Left-handed circular polarization. The helical trace of the point of the electric field vector makes a left-handed twist as seen from the source 'S'. (b) Right-handed circular polarization. The helical trace of the point of the electric field vector makes a right-handed twist as seen from the source 'S'. Image adapted from [9].

example, superchiral fields excited by plasmonic chiral metamaterials allow for ultra-sensitive bio-sensing [1]. The geometry of a helix has been calculated to be a very suitable geometry if a far-field chiral optical response is desired [14]. Gansel et al. studied the transmission of circularly polarized light through arrays of gold micrometer sized helices on a glass substrate [15, 16]. A broad dip in the transmittance of LCP in the micrometer wavelength regime was measured when an array consisting of left-handed helices was found. In the theoretical work, geometrical parameters that were expected to influence this transmission dip such as helix pitch, lattice constant, helix major radius, and helix minor radius were investigated one by one while keeping the other parameters constant. Strong transmission dips were found for dense arrays (either large major radius or small lattice constant), tall helices and small minor radii.

Thus, arrays of micrometer-sized gold helices are optically active in the micrometer regime since the transmission of LCP is smaller than the transmission of RCP. However, for applications using visible light, a similar optical response is needed in the visible wavelength regime. This has the consequence that helical structures with nanometer dimensions have to be fabricated. Fabrication of such three dimensional nanometer-sized complex geometries is a challenging process.

1.4 Thesis outline

In this thesis the fabrication of arrays of plasmonic nanohelices is discussed in Chapter 2. The important parameters that influence this fabrication are considered in detail. Chapter 3 focuses on transmission measurements of the arrays of plasmonic nanohelices. The optical activity measured in the transmission measurements validates success of the fabrication of the nanohelices. In Chapter 4, results from simulations are compared with the experimental results.

2 Fabrication of nanohelices

To investigate the optical response of a sample with plasmonic nanohelices, we develop a method to fabricate these nanostructures. Size and shape has to be controlled precisely using this fabrication method. By fabricating the nanohelices as a core-shell (silica-gold) geometry, extra optical tunability is possible by using different gold layer thicknesses. Since we expect a low signal from measurements on a single nanohelix and measurements on a single nanohelix are experimentally challenging, the nanohelices are fabricated in an array. The nanohelices are deposited on a glass sample, through which visible wavelengths can be transmitted. Using electron beam induced deposition followed by sputtercoating of gold, fabrication of the desired sample is possible.

There are many ways to deposit a material on a sample. In earlier work on helix fabrication, the helices were often a couple of micrometer in size. Using direct laser writing these helices could be fabricated using only gold, resulting in solid gold helices [16]. This method cannot be used to create nanometer sized helices due to resolution restrictions. Furthermore, glancing angle deposition was used to successfully fabricate Cu and Cu/Ag alloy nanohelices [17]. To date, fabrication of core-shell (silica-gold) nanometer sized helices has not been realized yet.

For depositing structures of nanometer size, a mechanism that can be controlled at the nanometer scale is necessary. A possible tool could be to use a beam of high energetic particles such as ions or electrons. In 1934, Stewart reported layer growth in his optical system at the location where the beam impinged on the sample surface [18]. He reported this ‘deposition’ as troublesome and something that should be avoided and did not mention, or perhaps notice, the possible benefits of this layer growth at such a small scale. It was not until in 1960 that Christy reported the possible benefits of thin film deposition created by electron bombardment [19].

During the following decades, deposition techniques using beams of high energetic particles were extensively explored with the goal of achieving a high resolution, a high deposition rate and a high purity of the deposited material. If an electron beam was used then the technique came to be known as (focused) electron beam induced deposition (F)EBID. Electron beam induced deposition is a technique with which a highly precise pattern can be defined on a substrate, since an electron beam can be made as small as 0.1 nm. Using this technique, nanostructures of less than 10 nm in size can be fabricated [20].

In the sections below, this unique fabrication method of the plasmonic nanohelices will be explained (Section 2.1) and the parameters of influence will be discussed (Section 2.2).

2.1 Electron beam induced deposition and sputtercoating

Electron beam induced deposition (EBID) is a bottom up lithography technique with which fine solid structures of several nanometers in size can be deposited on a sample. The basics of the deposition technique are straightforward. A precursor gas is introduced in the vacuum chamber of an electron microscope where a sample is present, often through a so-called gas injection system (GIS), as can be seen in Figure 2.1. The molecules in the precursor gas are partly adsorbed on the sample surface. At the location where the electron beam hits the sample, the precursor gas molecules are dissociated into volatile and non-volatile components as they interact with low energetic electrons at the sample surface. The non-volatile components will

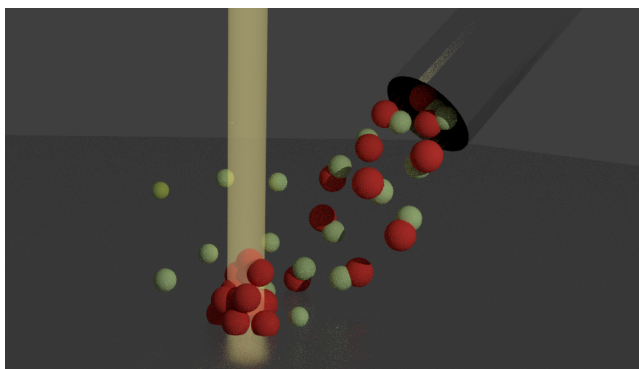


Figure 2.1: Artist impression of EBID. The gas injection system inserts precursor gas onto the sample, in this case consisting of volatile (green) and non-volatile (red) components. At the location where the electron beam (yellow) impinges on the sample, the non-volatile components are deposited. Volatile (green) components are removed from the vacuum system through pumping.

remain at the dissociation location and the volatile components are pumped out of the system with a vacuum pump.

The dissociation rate of the precursor gas molecules can be described as [21]

$$k_e = \sigma(E) \cdot \Gamma_e \left(\frac{\text{reactions}}{\text{s}} \right). \quad (2.1)$$

In Equation 2.1, the dissociation rate k_e , represents how many reactions take place every second, $\sigma(E)$ represents the dissociation cross section and Γ_e represents the electron flux. The dissociation cross section and the electron flux depend on the energy and the current of the electron beam respectively. Using specific precursor gasses, specific materials can be deposited. The sample, on which deposition takes place, should be conductive to prevent charging while it is exposed to the electron beam. In this work, the sample therefore consists of a 1 mm glass slab with on top of it a 15 nm layer of indium tin oxide (ITO), a conductive oxide that is transparent for visible wavelengths. The microscope used in this work is a scanning electron

microscope (SEM) produced by FEI Company, the FEI Helios Nanolab 600. It has beam energies ranging from 350 eV – 30 keV and a maximum beam current of 22 nA. The resolution of the Helios microscope is 0.9 nm at 15 keV.

2.1.1 Fabricating a nanohelix

In the presence of the precursor gas, deposition occurs where the electron beam impinges the sample. Scanning a pattern with the electron beam results into a deposition of some shape on a sample. This pattern can be transferred to the system using so-called streamfiles containing coordinates where the electron beam scans and a time indication how long the electron beam stays at a defined coordinate. For a detailed description of a streamfile, see Appendix A.

When attempting to create a three-dimensional helix using a streamfile, a method displayed in Figure 2.2 was used. In the x-y plane, the streamfile contains the coordinates of a circle repeated three times at the same position. The x and y coordinates are defined as

$$\begin{aligned} x &= R \cos \alpha \\ y &= R \sin \alpha \end{aligned} \quad (2.2)$$

where R is the radius of the circle that is desired and α is an angle from 0 to 2π . As one can imagine, scanning this circle three times can lead to producing a helix with three turns if the parameters are such that the deposition continues on top of the earlier deposited material and the structure starts growing in the z-direction. When repeating the fabrication of a nanohelix in the x- and y-direction, an array of nanohelices is formed. The lattice constant, the distance between the helices, can be defined in the streamfile. To achieve fabrication of these nanohelices, several parameters have to be fine-tuned precisely.

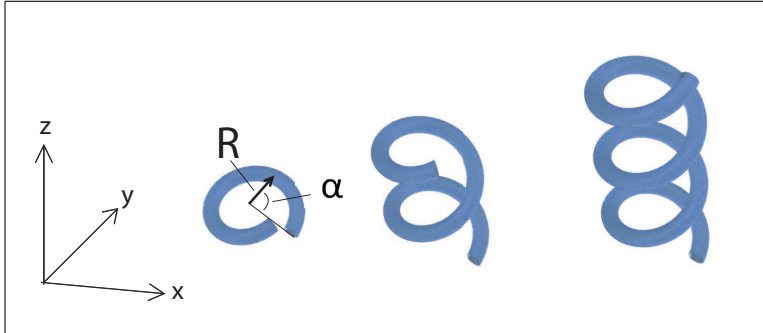


Figure 2.2: The method used to fabricate a nanohelix. The x-y plane corresponds to the field of view plane of the microscope. The streamfile contains the x,y coordinates of three circles per helix with a defined radius R and α going from 0 to 2π in a defined number of steps. Arrays are built up from in rows of constant x , going from high y to low y .

2.1.2 Electron beam energy

When the electron beam, containing primary electrons (PE), impinges on the solid sample, many interactions occur. These interactions can be elastic or inelastic and can influence both the primary electron energy as well as its trajectory. Typically, energy loss of the electron is caused by inelastic interactions and change of trajectory is caused by elastic interactions [21]. When an impinging primary electron hits an orbital electron of an atom in the sample, it loses a lot of energy. Less-energetic electrons ($E < 50\text{ eV}$) are called secondary electrons (SE). Secondary electrons are low-energetic electrons that assist the deposition. If an impinging primary electron reaches the nucleus of an atom in the sample, the electron does not lose much energy, but mainly is deflected in a very different direction due to the great difference in mass. These high-energetic electrons ($E > 50\text{ eV}$), are called backscattered electrons (BSE). A typical energy distribution of electrons emitted from a sample around the spot of the electron beam can be seen in Figure 2.3a. Many low energy secondary electrons are formed.

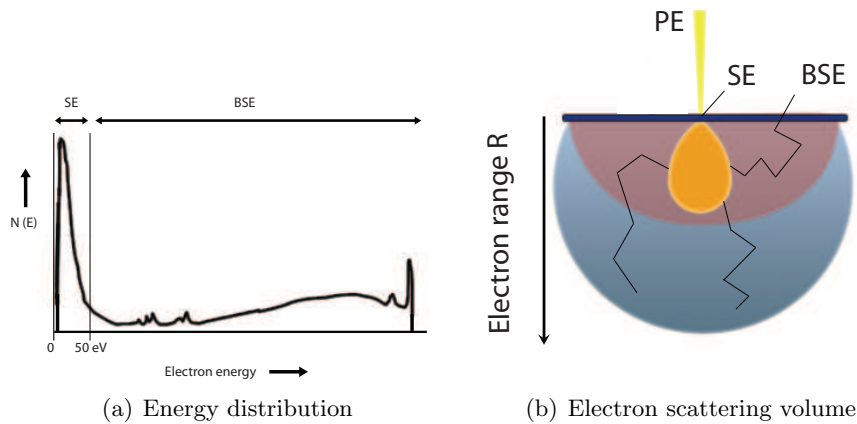


Figure 2.3: (a) The typical energy distribution of electrons that exist after a primary beam hits the surface of the sample. On the x-axis, the electron energy is given, on the y-axis, the number of electrons with a certain energy $N(E)$ is given. As can be seen, many low energetic secondary electrons (SE) are formed. (b) Typical scattering volume of a primary beam (containing primary electrons (PE)) that impinges on a sample surface. A small volume of secondary electrons is formed in proximity of the initial PE beam. Secondary electrons that exist close to the surface can escape and assist the deposition. Back scattered electrons (BSE), with higher energies, can travel further away from the initial PE beam, which leads to a larger scattering volume. Images adapted from [22].

All electrons that scatter somewhere under the sample surface form a typical scattering volume, as can be seen in Figure 2.3b. Higher energetic electrons can travel farther through the sample than less energetic electrons. Only the low energy secondary electrons that are close to the sample surface will be able to reach the sample

surface and assist the deposition. The scattering volume typically depends on the atomic number of the atoms, the density of the sample and the energy of the primary electrons. It can have a diameter ranging from 10 nm to 10 μm [22].

Thus, the scattering volume can be changed by a factor of 1000, depending on the beam energy, and this greatly influences the deposition. In Figure 2.4, we show the difference in the size of the scattering volume is displayed as a function of beam energy for the sample that is used in this work. The blue lines in Figure 2.4 show the primary electron trajectories that we calculated using CASINO, a software based on Monte Carlo calculations. As can be seen in Figure 2.4a and b, the scattering volume

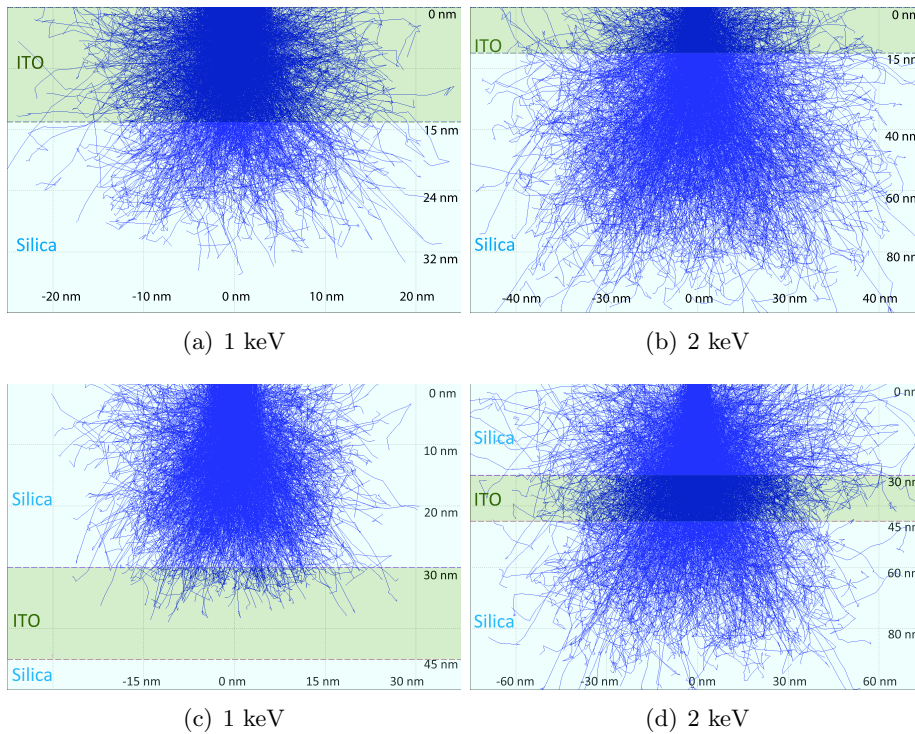


Figure 2.4: Scattering volume of an electron beam impinging on a substrate for different beam energies made using CASINO, a software that uses Monte Carlo calculations to determine electron trajectories. For (a),(b),(c) and (d), the substrate consists of 1 mm thick silica slab covered with a layer of 15 nm indium tin oxide (ITO). a) Scattering volume for primary beam energy of 1 keV. b) Scattering volume for primary beam energy of 2 keV. c) Scattering volume for primary beam energy of 1 keV. On top of original ITO layer, a 30 nm thick layer of silica is added representing already deposited material. d) Scattering volume for primary beam energy of 2 keV. On top of original ITO layer, a 30 nm thick layer of silica is added representing already deposited material.

increases with increasing beam energy. Consequently more secondary electrons will be formed farther away from the primary beam as there is a larger chance of inelastic interactions taking place farther away due to longer traveling distances of primary

electrons. Comparing the scattering volumes for 1 keV and 2 keV, it can be seen that the width of the scattering volume at the surface is about 10 nm and 20 nm respectively. Low-energy beams therefore, guarantee a higher precision than higher energy beams since the area in which electrons cross the surface is smaller. When an electron crosses the sample surface it can interact and dissociate an adsorbed precursor molecule.

2.1.3 Electron beam current

Since many different beam currents are available in the microscope used in this work, we investigate which beam current enables nanohelix deposition. As described in Equation 2.1, the dissociation rate and thus deposition rate, depends linearly on the beam current through the flux of electrons. When more electrons are available due to a higher beam current, the dissociation rate will increase. Since the currents in the microscope have fixed values, the beam current can only be tuned by factors of about two. In the pA regime for instance, 21 pA, 43 pA and 86 pA were currents that were used for successful deposition of nanohelices. These differences change the deposition drastically. Large changes in beam current can somewhat be compensated for, by the dwell time that can be tuned in fine steps. For instance, if a beam current of 21 pA combined with a dwell time of 14 ms and a stepsize of 4.56 nm results in short helices of ~ 400 nm, a beam current of 43 pA combined with a dwelltime of 14 ms will result in tall helices of $\sim 1\mu\text{m}$. Changing the dwell time to 10 ms in combination with the beam current of 43 pA could result in a helix with a moderate height.

2.1.4 Gas injection system

A gas injection system (GIS) is installed on the microscope in order to perform electron induced deposition. For deposition of silicon dioxide, the precursor tetra ethyl ortho silicate (TEOS) in combination with water vapor is used. The deposited material is also referred to as SiO_x , a silica-like oxide with an imperfect crystalline structure, in that not every Si-atom is bonded to exactly two O-atoms. Even so, in this thesis, the deposited material will be referred to as silicon dioxide. TEOS consists of a silicon atom and four OC_2H_5 groups. A few grams of liquid TEOS are located in a crucible in the GIS.

The GIS can only contain one chemical, in this way there is no risk of contamination of other chemicals. The TEOS in the crucible evaporates and the gas precursor is formed. The vapor pressure is built up until the saturated vapor pressure is reached. The temperature of the crucible is kept constant with the result that the pressure in the crucible is also constant. The flow of molecules into the vacuum chamber therefore is only dependent on what the saturated pressure is and what the flow resistance is into the vacuum chamber, both constant parameters, with the result

that the flow is also constant. This flow is set to a level at which the pressure is not too high for the vacuum system to still function. In the TEOS case, the pressure is $\sim 1 \cdot 10^{-5}$ mbar. Water vapor is added from an external source and is brought together with the TEOS vapor right before the gas enters the vacuum chamber. The water molecules are necessary to add extra oxygen atoms to the gas, so enough oxygen atoms are available for the deposition of silicon dioxide. With water vapor added, the pressure rise in the vacuum chamber is on the order of $3 \cdot 10^{-5}$ mbar. Compressed air is used to insert the GIS into the vacuum chamber, the movement of the GIS is therefore very fluent and the precursor liquid is barely shaken. A needle, with a diameter of $\sim 300 \mu\text{m}$ can be brought close ($\sim 100 - 150 \mu\text{m}$) to the sample with the consequence that the precursor gas is only present on a small area of the sample.

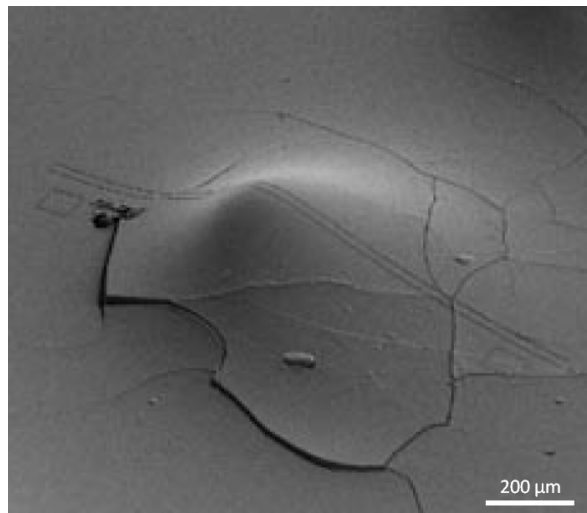


Figure 2.5: SEM picture where height represents the density profile of a precursor gas. The sample surface was cooled to -150°C . From the gas injection system, located at the top left corner of the image, the precursor gas flowed onto the sample and immediately froze. Two parallel lines were milled into the frozen precursor to show the difference in height of frozen precursor on the sample. This difference in height represents the density of the precursor gas on the sample. Image courtesy of FEI, www.fei.com [23].

Even though the precursor gas is presented to the sample locally, the surface area covered by molecules is relatively large and has a radius of about 0.5 mm. In Figure 2.5 an example is shown of frozen precursor on a sample surface taken from [23]. Note that the GIS needle is directed from the top left corner towards the bottom right corner of the image. In order to make this SEM picture, the sample surface was cooled to -150°C and the precursor gas froze immediately when presented to the sample surface. The SEM image displays the height of the frozen material and this is linearly proportional to the gas density at every location. Two lines were milled into the frozen precursor to show the difference in height of frozen precursor. The measurement showed that the gas density homogeneity over a distance of $< 100 \mu\text{m}$

is better than 6% [23]. According to the developers of the precursor system, homogeneity is to be considered constant over several micrometers. This is different from what we have experienced in the process of depositing arrays of nanohelices. When making an array of roughly $10\mu\text{m} \times 10\mu\text{m}$, the helices in the top left corner, closest to the GIS, consistently became larger than the helices at the bottom right of the array. This is attributed to inhomogeneity in the surface coverage of the precursor, even though the array is much smaller than $100\mu\text{m}$ in length. Another reason could be that previously deposited helices shadow the precursor gas from reaching areas where helices are deposited at a later moment.

2.1.5 Stepsize and dwell time

The parameters that are determined in the streamfile are the stepsize and the dwell time. The circle that is scanned by the electron beam, as discussed in Section 2.1.1, can be traced using a variable amount of steps. Using many steps will decrease the stepsize and using few steps will increase the stepsize. The x- and y-coordinates are determined by α , that ranges from 0 to 2π , and this range can be divided in any number of angles and for each of these angles a x- and y-coordinate can be determined. When the steps are small enough that, in every step, the beam position overlaps with that of the previous step, the deposition (partly) occurs on top of the previously deposited material. This way, the helix starts growing in the z-direction. The dwell time determines how long the electron beam stays at one position. When the beam is stationary for a longer time, more material is deposited at that location.

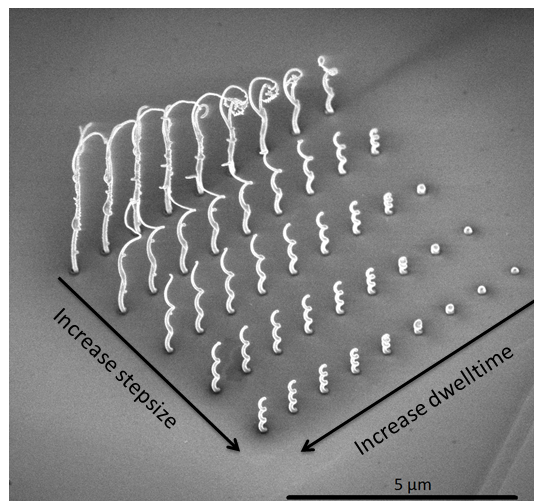


Figure 2.6: SEM picture of an array of different helices fabricated using different dwell times and stepsizes. The sample is rotated (50°) and tilted (45°). The structures were made with a beam energy of 1 keV and a beam current of 43 pA. Dwell time and stepsize were varied as indicated by the arrows. The dwell time ranges from 5 ms to 21 ms in steps of 2 ms. The stepsize ranges from 0.76 nm to 3.80 nm in steps of 0.76 nm.

In Figure 2.6 the influence of the stepsize and the dwell time is shown. If the stepsize is small, the deposition will grow faster in the z-direction than in the x- or y-direction. This results in a pillar almost going straight upwards as can be seen in the top left of Figure 2.6. If the dwell time is short, the deposition doesn't work out due to the fact that not enough material is deposited in the short amount of time. This results in a droplet of material as can be seen in the bottom right of Figure 2.6. But somewhere in between, combinations of a certain dwell time and stepsize lead to well defined nanohelices.

2.1.6 Sputtercoating with gold

In order to make the particles metallic and therefore plasmonic, the SiO_x nanohelices have to be coated with gold. The most isotropic method available is using a sputtercoater, as opposed to evaporation of gold which is much more directional (from the top down). The sputtercoater used has an argon discharge plasma for diffusive deposition. A gold target delivers the gold ions. Examination of the sputtercoated

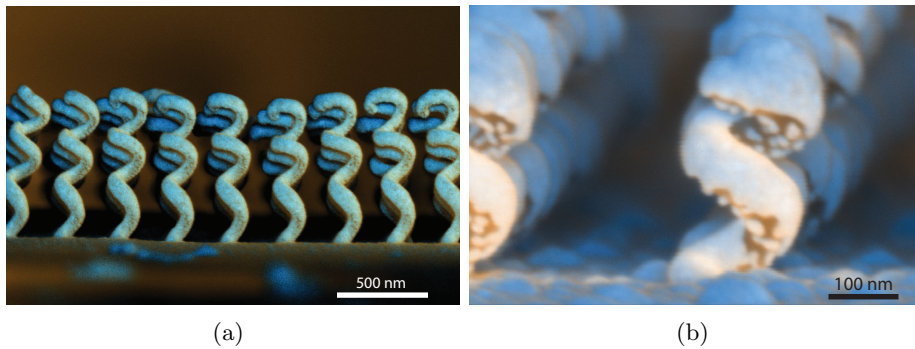


Figure 2.7: Two SEM images of nanohelices from the array used in the transmission measurement sputtercoated with gold. Different colors represent different materials. From both (a) and (b) it becomes clear that the sputtering is homogeneous on top of the nanohelices but not at the bottom of the curves of the nanohelices. The top of the helix seems to shadow the bottom of the helix.

helices in an electron microscope revealed that the sputtercoating was not fully homogeneous. In Figure 2.7 the homogeneity of the gold layer can be examined by looking at the different colors. By using a mix of the images made with two different detectors, a secondary electron detector and a backscatter electron detector, an image can be made in which different colors represent different materials. Looking at the bottom of the curves of the helices shows that the gold layer is not fully homogeneous there. In Figure 2.7a, tall and thin nanohelices are displayed and in Figure 2.7b, the nanohelices are shorter and a bit thicker. In Figure 2.7a dark areas can be seen at the bottom of the curves. These dark areas are SiO_x in contrast to the light color that represents gold. In Figure 2.7b, the light colored gold patches are

clearly visible on the dark surface of SiO_x . These images suggest that the top of the helices overshadow the bottom side of the helices during the sputtering of the gold.

2.2 Delicate interplay between factors

As described in the section above, parameters as beam energy, beam current, dwell time, stepsize and location of deposition in the writing field are of great influence on deposition results. With the aforementioned knowledge we managed to successfully fabricate nanohelices in a controlled manner, as can be seen in Figure 2.8, where the left picture presents an overview and the right picture a close-up of the fabricated sample. Although we can control these specific parameters, very subtle changes, for example, in the temperature of the substrate due to e-beam induced heating, fluctuations in the gas pressure, the precursor residence time on the substrate, or background pressure changes can influence the deposition in small ways that are sometimes unpredictable.

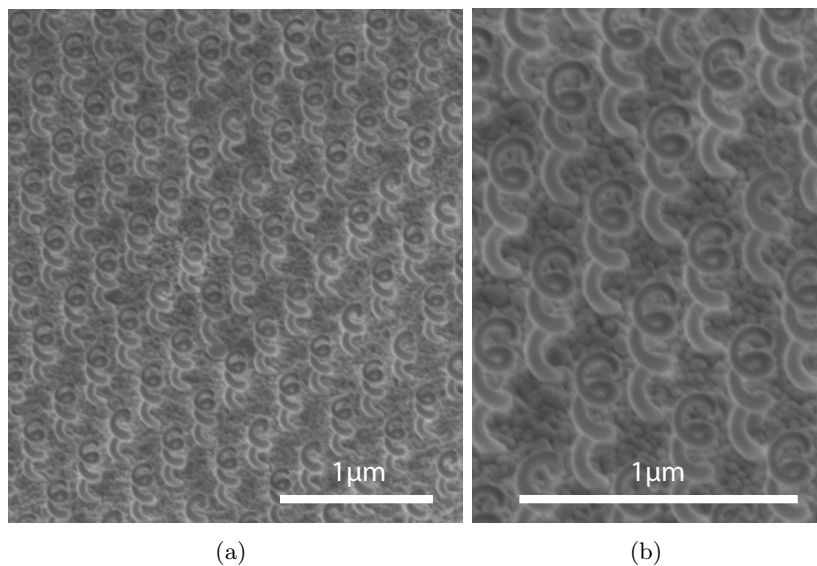


Figure 2.8: SEM pictures of the fabricated sample. The left image is an overview and the right image is a close-up of some nanohelices. The parameters used for deposition were a beam energy of 1 keV, a beam current of 21 pA, a dwell time of 14 ms, a magnification of 5140x which corresponds to a pixelsize of 0.76 nm, a stepsize of 4.56 nm and a lattice constant of 400 nm. During deposition the pressure of the vacuum chamber was $1.38 \cdot 10^{-5}$ mbar. The sample was sputtercoated with 40 nm of gold using a current of 90 mA. The helices consist of three turns

All successfully fabricated nanohelices required a low beam energy of 1 keV. This low energy ensured a small scattering volume of the electrons (Figure 2.4), and a very high accuracy of deposition. A small scattering volume also guaranteed that while

depositing the helical geometry no deposition could take place under the just formed turn, since the scattering volume is fully inside the previously deposited structure. Furthermore, the beam current was also quite low during deposition. The beam currents used for successfully fabricated nanohelices were 21 pA, 43 pA and 86 pA. The stepsize used was between 1 and 10 nm and the dwell times around 15 ms.

The lattice constant of the arrays of nanohelices can be set to values as small as 300 nm resulting in dense arrays. The separate helices have comparable heights and major and minor radii. In Figure 2.8, the sample that is used in the experiment is displayed. As can be expected with such a delicate fabrication method, approximately 1 in every ~ 25 helices deviates from its neighbors, which is not expected to have a significant effect on the transmission measurements.

3 Optical measurements

3.1 Sample characterization

Transmission measurements are performed on a periodic array consisting of 1088 (32×34) left-handed core-shell nanohelices with a silicon dioxide core and gold shell fabricated in the manner described in Chapter 2. The total measurements of the array are $13.6 \mu\text{m} \times 12.8 \mu\text{m}$. A topview of this sample can be seen in Figure 3.1.

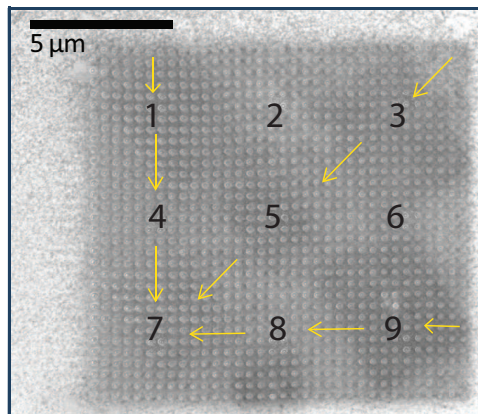


Figure 3.1: SEM image of the topview of the fabricated sample. The array consists of 1088 core-shell nanohelices. The measurements of the array are $13.6 \mu\text{m} \times 12.8 \mu\text{m}$. While fabricating the sample, the gas injection system was directed from top left to bottom right. The numbers represent nine different locations at which measurements were performed. The yellow arrows display the increase in helix height in the array.

Using the knowledge that the direction of the gas injection system direction influences the height of the fabricated helices, we fabricate an array in which the helix height varies. In Figure 3.1, the GIS is directed from the top left to the bottom right. The gradient of helix heights, indicated with the yellow arrows in 3.1, is exploited to investigate if optical activity changes as a function of helix height. Using the measuring tool in the microscope, we measure the helix heights while tilting the sample at 45° . For every measuring location, represented by the numbers in Figure 3.1, helix heights from four areas around the measuring location are averaged. These areas are displayed in Figure 3.2. For example, to determine the height of location 1, an average of the helix heights in pink areas a,b,c and d is taken. Area d is also used for the calculation of the average height of the helices for location 5, displayed in grey. This method gives a representative overview of the gradual distribution of helix heights throughout the array. The error on this height measurement is determined by calculating the standard deviation of the set helix heights from the four areas.

The helix heights vary from $546 \text{ nm} \pm 92 \text{ nm}$ to $766 \text{ nm} \pm 46 \text{ nm}$. The nine different averaged heights with corresponding standard deviations we use in our measurements are displayed in Table 3.1. In Figure 3.3, SEM images of helices with different heights are displayed. Here can be seen that all helices are nicely formed but that the height of the helices clearly differs.

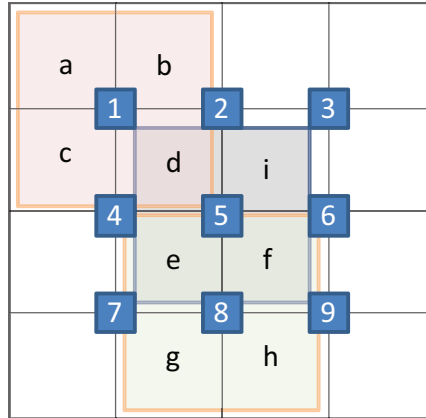


Figure 3.2: Using the measurement tool of the microscope, it is possible to measure the heights of the helices. The numbers represent the locations at which measurements are performed. After dividing the array into 16 areas, the average helix height is determined using helix heights from the 4 areas directly surrounding each measurement location, for location 1 these are the pink areas a,b,c and d. The standard deviation is determined for the set of helix heights which is averaged over for each location.

Helix heights		
(1) $705 \text{ nm} \pm 26 \text{ nm}$	(2) $666 \text{ nm} \pm 50 \text{ nm}$	(3) $546 \text{ nm} \pm 92 \text{ nm}$
(4) $730 \text{ nm} \pm 24 \text{ nm}$	(5) $686 \text{ nm} \pm 40 \text{ nm}$	(6) $577 \text{ nm} \pm 81 \text{ nm}$
(7) $766 \text{ nm} \pm 46 \text{ nm}$	(8) $695 \text{ nm} \pm 55 \text{ nm}$	(9) $582 \text{ nm} \pm 70 \text{ nm}$

Table 3.1: The average helix heights at nine different locations on the array where measurements are performed. The error given is the standard deviation of the set of helix heights that is averaged over. In Figure 3.1 and 3.2, the corresponding locations can be seen.

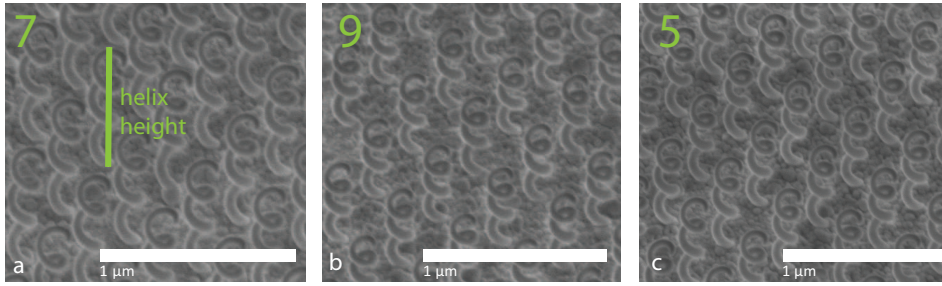


Figure 3.3: Different close-up SEM images of the nanohelices on different locations on the array. The green numbers correspond to their locations in Figure 3.1. The green line in a) represents a helix height measurement. In the image, the helices are not sputtered with gold yet. a) Helix heights of ~ 766 nm. b) Helix heights of ~ 582 nm. c) Helix heights of ~ 686 nm.

3.2 Experimental setup

In order to measure optical activity in the visible wavelength regime, transmission measurements are performed through the array of helices using the setup displayed in Figure 3.4. The light source is a supercontinuum white light laser that provides a broad set of wavelengths in the visible wavelength regime. In order to circularly polarize the light, as described in Section 1.3, we first fix the polarization using a linear polarizer (LP) for visible wavelengths. Using an achromatic quarter wave plate ($\lambda/4$), also for a broad range of visible wavelengths, positioned at an angle of $\pm \pi/4$ with respect to the linear (horizontal) polarization, the light is either polarized right-handed circularly or left-handed circularly. Switching the quarter wave plate from $-\pi/4$ to $+\pi/4$ with respect to the horizontal linear polarization changes the polarization from right-handed circular to left-handed circular respectively. Spectra are taken using a grating spectrometer for visible wavelengths from $\lambda = 600$ nm to $\lambda = 950$ nm.

At every location on the array as displayed in Figure 3.1, the array is illuminated by both left-handed and right-handed circularly polarized light. As displayed in Figure 3.4, a $40\times$ objective with an NA of 0.65 is used to focus the laser onto the gold surface of the sample to a spot with a full width half maximum (FWHM) of $\sim 3\mu\text{m}$. Note that the yellow part of the sample represents the gold side with the helices. A second $40\times$ objective collects the illuminated area of similar FWHM from the sample surface. From there the signal is spectrally analyzed by a grating spectrometer. The back-illuminated CCD in the grating spectrometer is known to exhibit Fabry-Perot type fringes for high wavelengths. A lamp, a pellicle beam splitter on a flip mount and a flip mirror are used to make a reflection path, which can be used to locate the spot on the sample between measurements. When performing the measurements, these components are flipped out of the path of the laser. Using the setup described above and presented in Figure 3.4, spectra were taken at the nine different locations on the nanohelix array as described in Section 3.1.

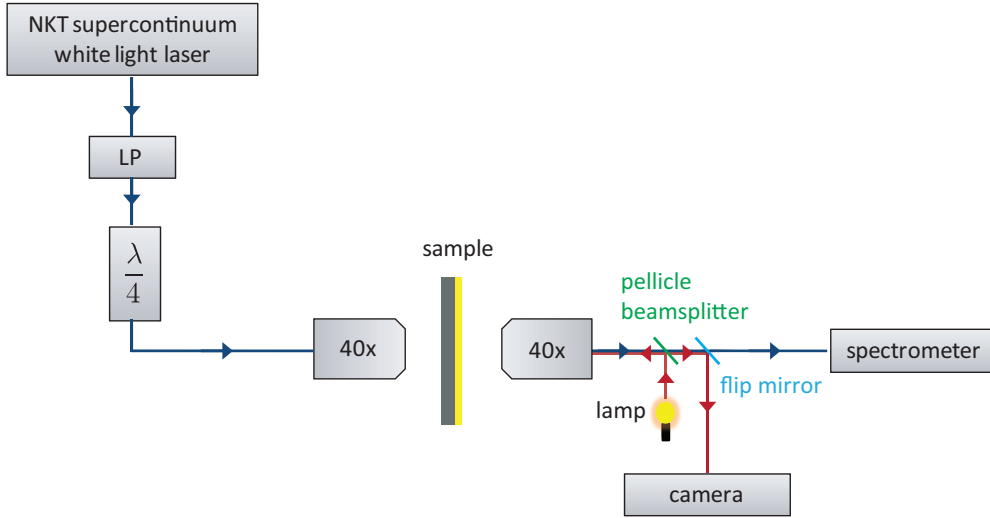


Figure 3.4: Schematic of the experimental setup used for the transmission measurements. The source is a supercontinuum white light laser that provides a broad set of wavelengths. Using a linear polarizer combined with a quarter wave plate, the light is circularly polarized. Using an objective the light is focused through the glass side of the sample on the gold nanohelices. Using a camera combined with a lamp, a pellicle beamsplitter on a flip mount and a flip mirror, we can locate where the spot is on the array. Using a grating spectrometer, spectra can be taken.

3.3 Results

At the nine different locations, the sample is illuminated with both LCP and RCP. As a reference measurement, sets of spectra were also taken on the flat gold film in the proximity of the nanohelix array. Figure 3.5 presents transmission spectra as a function of wavelength for helices with a height of $666 \text{ nm} \pm 50 \text{ nm}$ for the two different polarizations, LCP and RCP. The spectra in Figure 3.5a show the transmission of LCP and RCP through a location of the nanohelix array represented by the green and blue line respectively. In Figure 3.5b, the transmission of LCP and RCP through the flat gold film next to the array is displayed and represented by the green and blue line respectively.

We observe a difference in the curves representing RCP and LCP in Figure 3.5a. Around $\lambda = 700 \text{ nm}$, the transmission data of LCP and RCP diverge. This is not the case in the transmission data through the flat gold film presented in Figure 3.5b. Here the transmission data of LCP and RCP mostly overlap. The difference in transmission between LCP and RCP through the nanohelix array indicates optical activity.

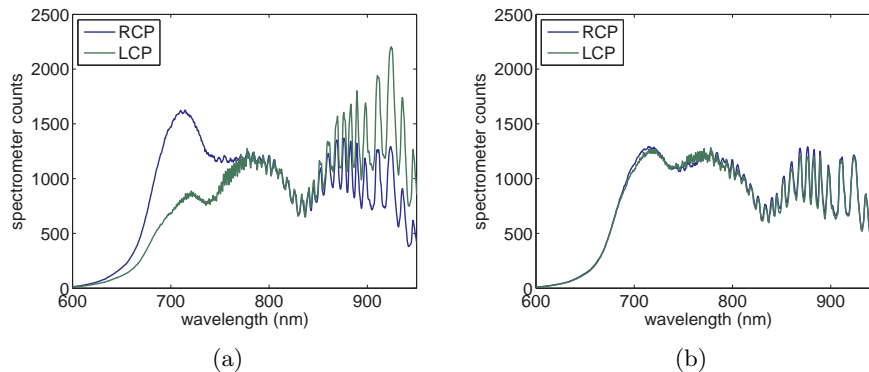


Figure 3.5: Transmission data as a function of wavelength. (a) The transmission data of transmission through the nanohelix array with RCP (blue) and LCP (green). (b) The transmission data of transmission through the flat gold film with RCP (blue) and LCP (green).

We observe a difference in the intensity of the signal of RCP light between Figure 3.5a and b. Around $\lambda = 700\text{nm}$, the intensity of RCP light through the flat gold film is lower than through the array of nanohelices. In contrast, we had expected that the signal through the array of nanohelices would be lower due to the extra gold that the light would have to penetrate. Through the flat film (b), the light only has to travel through the gold layer and in the case of the nanohelix array, in addition to the gold layer, light also has to travel through the gold coated helices. Here we see that this is not the case: the intensity of the transmission through the array is a bit higher than the transmission through the flat gold film. Additionally, when using randomly polarized light, we consistently observed a higher transmission through the array of nanohelices than through the flat gold film for visible wavelengths. We expect this has the reason that the sputtercoating was more successful next to the array than in the array of nanohelices. Shadowing effects as discussed in Section 2.1.6 probably play a role in the formation of the gold layer in between the helices. Since the area that has to be covered in the nanohelix array is significantly larger than the area of the flat gold film, less gold is available for covering everything in the array and thus the gold layer is thinner. This thinner gold layer results in a higher transmittance of the nanohelix array compared to the transmission of light through the flat gold film.

The transmission data can be converted to optical activity using Equation 1.4. Since the helices are left-handed, we expect that LCP light is transmitted less well than RCP light, based on the micrometer helices studies of Gansel et al. [15]. The low transmission of LCP light results in a dip in the optical activity curve as a function of wavelength.

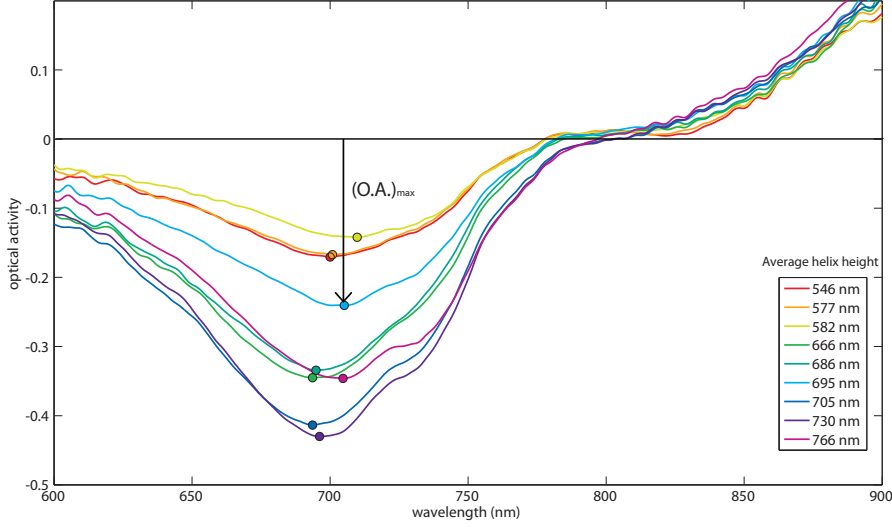


Figure 3.6: Optical activity as a function of wavelength for different helix heights calculated with Equation 1.4. Different colors represent different helix heights. For each curve, the minimum value in the dip is defined from zero down resulting in nine different values of $(O.A.)_{\max}$.

In Figure 3.6, we observe a dip in all the curves, meaning that for a range of wavelengths, $T_{LCP} < T_{RCP}$ which is what we expected for left-handed helices. The location of the dip is in the visible, at $\lambda \sim 700$ nm. Thus, this dip represents optical activity in the visible wavelength regime on the array plasmonic nanohelices. The optical activity of the different curves have large values up to $\sim 45\%$. Furthermore, we observe that the size of the dip varies with helix height. For a helix height of 546 nm, the dip has a value of ~ -0.12 and for a helix height of 730 nm, the dip has a value of ~ -0.46 , which is higher with a factor of about 3. To study these dips in more detail, the minimum value in each dip is determined from zero down and called $(O.A.)_{\max}$.

The maximum optical activity as a function of helix height is displayed in Figure 3.7. The errorbars represent the standard deviations from Table 3.1. We observe a trend: optical activity increases with helix height.

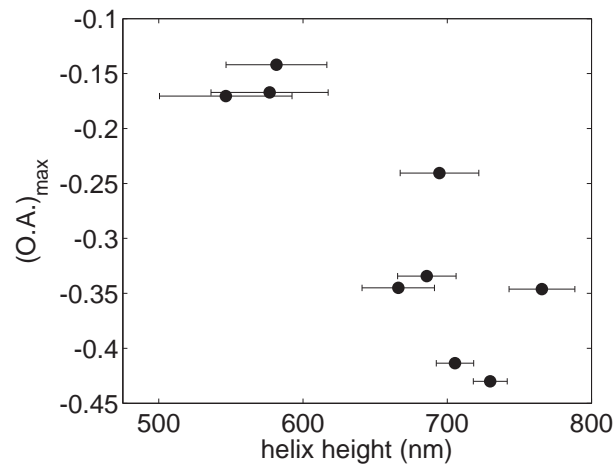


Figure 3.7: Maximum optical activity as a function of helix height for the experimental data. The errorbars correspond to the standard deviation of the helix height sets (see Table 3.1 for the values and Section 3.1 for the explanation). We recognize a trend in which shorter helices have smaller maximum optical activities than taller helices.

4 Numerical calculations

In order to understand and check the results achieved in the experiment and shown in Chapter 3, we compare these results to theoretical calculations. Therefore, COMSOL Multiphysics (version 4.4) is used to model the optical activity of plasmonic nanohelices. COMSOL Multiphysics is software based on Maxwell's equations and uses finite element modeling [24].

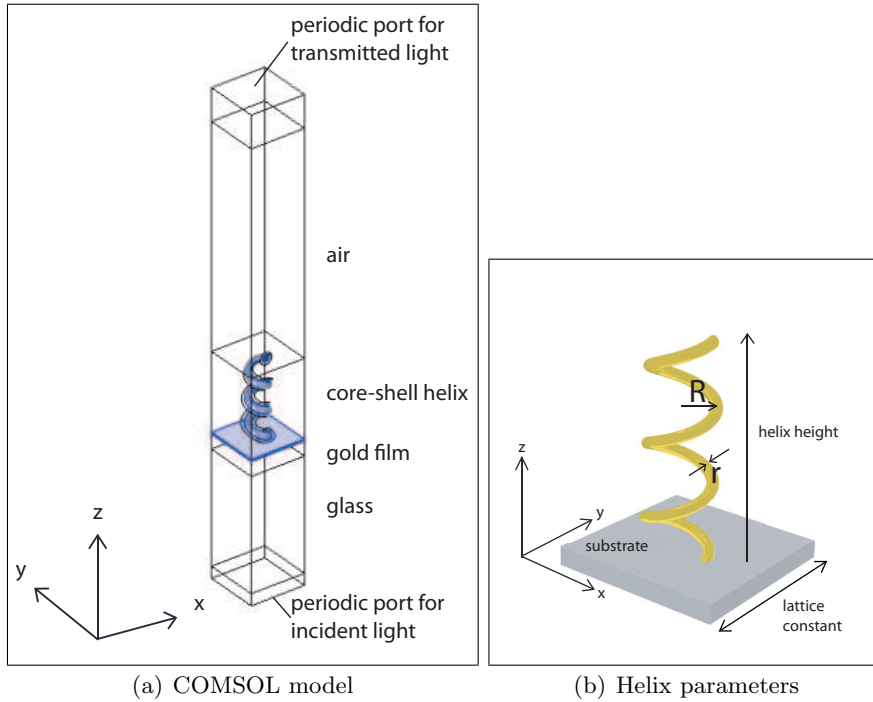


Figure 4.1: (a) The COMSOL model designed to calculate transmission through an array of left-handed core-shell (silica-gold) nanohelices on top of a glass substrate. Using periodic boundary conditions in the x -direction and y -direction, the single defined helix becomes an array of identical helices. In purple are the domains made of gold; the shell of the helix and the thin layer on the sample. (b) A right-handed helix on a substrate with the parameters as defined in COMSOL. Major radius R , minor radius r and the helix height are shown.

4.1 Model description

A three-dimensional model is designed as shown in Figure 4.1a. A core-shell (silica-gold) helix is located on top of a thin gold film on a glass substrate. The gold shell of the helix and the thin gold layer on the glass sample are depicted in purple. Data from Johnson and Christy [25] is used for the optical constants of gold. The calculation box has periodic boundary conditions in the x -direction and y -direction. This calculation box is therefore the unit cell that is repeated in the x - and y -direction. This has the

advantage that only one helix has to be defined in the model while calculations are performed on an array of helices. The lattice constant of the array is equal to the sides of the box in the x- and y-direction, in this case the distance is taken to be the same in both directions. The helix geometry exists as a standard geometry in COMSOL and can be chosen to be either right-handed or left-handed. Furthermore, the total height of the helix, its major and minor radius can be defined, and these basic helix parameters are shown in Figure 4.1b. Two separate helices are defined to create the core-shell structure. The inner made of silica and the outer made of gold. These helices have the same major radius but different minor radii. The difference in minor radii is the thickness of the gold shell. This thickness chosen for the gold shell is also the thickness of the gold layer on the glass sample, since in the experiment these layers are deposited at once by sputtering.

The finite elements are determined by the mesh. A tetrahedral mesh is used throughout the unit cell that is very fine in the proximity of the helix and increases in size farther away from the helix. Around the core-shell helix, a helix made of air is added to the model as a trick to have the possibility to locally define an extreme fine mesh in the air at the gold-air interface. Furthermore, boundary layers were used to define an extreme fine mesh in the gold at the gold-air interface.

At the top and bottom of the calculation box, two periodic ports are defined. At such a periodic port, the electromagnetic energy can either enter or exit the model. In this case, the bottom periodic port (glass side) excites circularly polarized light and the top periodic port (air side) receives the transmitted light. Note that the bottom port also receives reflected light. The circularly polarized light propagates in the positive z-direction and can be chosen to be left-handed or right-handed circularly polarized by defining the x- and y-components of the electric field using the Jones vector representation [9] as

$$\mathbf{E}_{\text{LCP}} = \left(\frac{1}{\sqrt{2}}, \frac{i}{\sqrt{2}}, 0 \right) \quad (4.1) \quad \mathbf{E}_{\text{RCP}} = \left(\frac{1}{\sqrt{2}}, \frac{-i}{\sqrt{2}}, 0 \right) \quad (4.2)$$

where $\mathbf{E}_{\text{LCP(RCP)}}$ represents the electric field vector of LCP (RCP).

To investigate the influence of helix height on optical activity, calculations are done for four different helix heights, 600 nm, 700 nm, 800 nm and 900 nm. The choice is made to perform the calculations on an array of left-handed helices to make sure that calculations are in agreement with the experiment. The helices in the calculations have a major radius of 90 nm, a minor core radius of 15 nm, a gold shell thickness of 20 nm and a gold layer on the substrate of 20 nm. The lattice constant of the array is 600 nm, which is bigger than the lattice constant used in the experiment. The reason for this is a practical one: when decreasing the lattice constant to smaller values than 600 nm, a problem occurred in meshing the system.

4.2 Results

A parametric sweep is done over wavelengths from $\lambda = 610$ nm to $\lambda = 950$ nm in steps of 10 nm and this calculation is subsequently performed with LCP and RCP incident light.

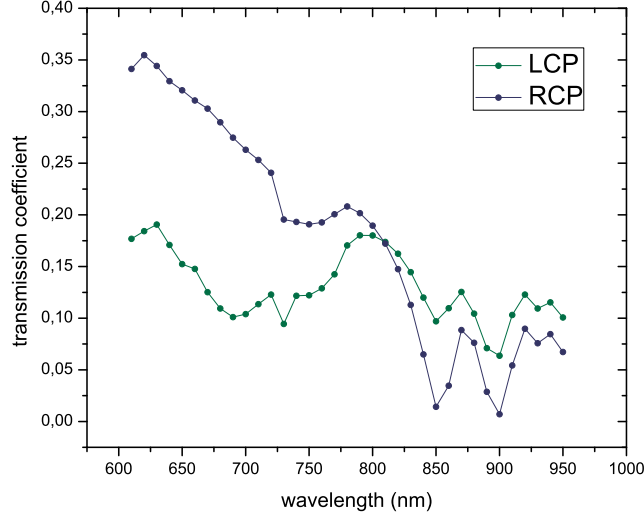


Figure 4.2: Calculated transmission coefficients for an array of helices with a height of 700 nm as a function of wavelength. Blue represents the transmission of RCP and green represents the transmission of LCP.

From the calculation, the transmission and reflection coefficients are extracted. Furthermore, the absorption in the gold layer on the substrate and the gold shell of the helix are derived separately. In Figure 4.2, the transmission coefficients calculated for LCP and RCP are displayed as a function of wavelength. Using these transmission coefficients and Equation 1.4, we determine the optical activity. An example of one of the four optical activity graphs is given in Figure 4.3. In this figure, the optical activity is displayed as the function of the wavelength. At small wavelengths, the optical activity is below zero, which means that the transmission of LCP is lower than the transmission of RCP, $T_{LCP} < T_{RCP}$ in Equation 1.4. This dip is located around $\lambda = 700$ nm and has a large value of about 50%. At larger wavelengths, the optical activity rises above zero and two peaks at $\lambda = 850$ nm and $\lambda = 910$ nm with values up to 80% appear. These peaks are very unexpected and to date, the reason for these dips is unknown. Overall, the optical activity graph has a strong resemblance of the experimental results described in Chapter 3 since the curves show similar qualitative behavior.

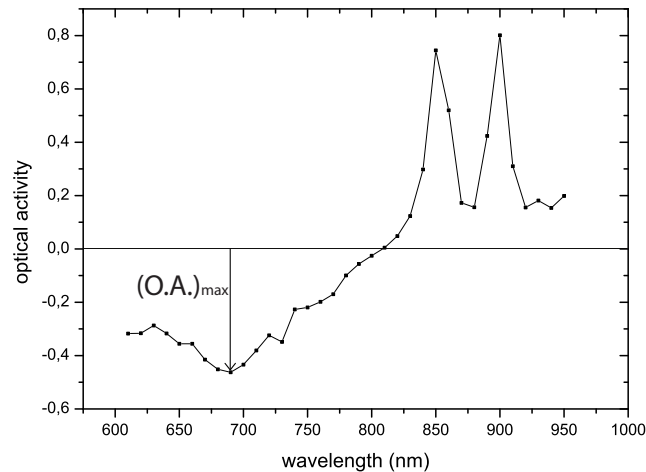


Figure 4.3: Optical activity as a function of wavelength determined with transmission data derived from the COMSOL calculations for a helix height of 700 nm. A parametric sweep was done over wavelengths from $\lambda = 610$ nm to $\lambda = 950$ nm in steps of 10 nm for LCP and RCP. The points in the graph are the thirty-five data points that were calculated. From zero down the value $(O.A.)_{\max}$ using the data point with the lowest value.

The optical activity curves for helix heights of 600 nm, 800 nm and 900 nm have the same shape as the curve displayed in Figure 4.3. To be able to study the size of the dips in optical activity for four helix heights in the calculations, $(O.A.)_{\max}$ is defined as described in Section 3.3. To determine $(O.A.)_{\max}$, the optical activity data point with the lowest value is chosen. The maximum optical activity as a function of helix height is displayed in Figure 4.4. We observe a similar trend as in the experimental results: for short helices, the maximum optical activity is smaller and for tall helices, the maximum optical activity is large.

The values of $(O.A.)_{\max}$ are large up to $\sim 65\%$ for a helix height of 900 nm. A helix height of 600 nm deviates from this trend, with a large maximum optical activity. Up till now we have the expectation that this might be due to the fact that for a helix height of 600 nm, the helix height and lattice constant are equal and this might initiate an unexpected effect in the COMSOL model. Since in the experiment, all helices that are measured on are taller than the lattice constant, we mainly focus on the calculation data of the helices that are taller than the lattice constant. The trend for these heights corresponds well to the trend observed in the experimental results.

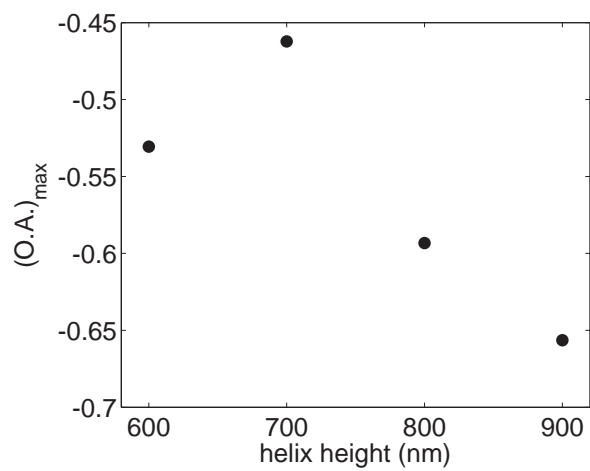


Figure 4.4: Maximum optical activity as a function of helix height for the calculation data. Calculations are done for four different helix heights.

5 Discussion and Outlook

5.1 Comparison experiment with calculations

For both experimental data (Chapter 3) and calculated data (Chapter 4), we observe a large dip in the optical activity around $\lambda = 700$ nm. This indicates that we measure large optical activity on an array of plasmonic nanohelices. It is reasonable to expect that, due to some differences between the experiment and the calculation, the results do not show perfect quantitative agreement.

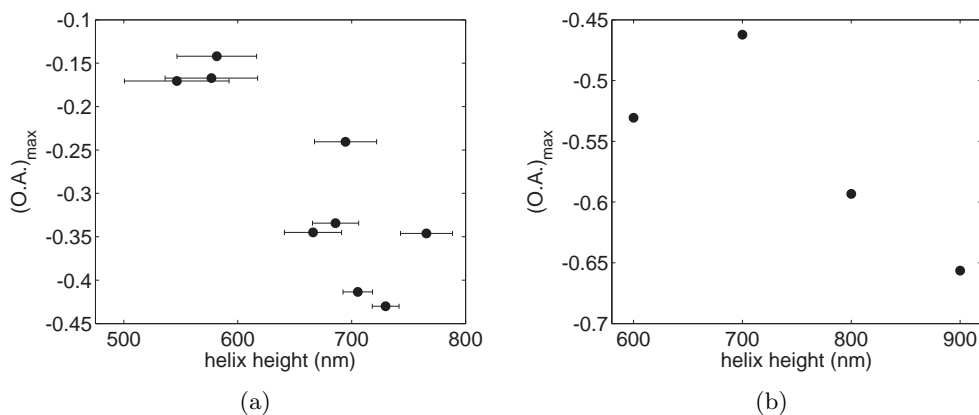


Figure 5.1: (a) Maximum optical activity as a function of helix height for the experimental data. Errorbars correspond to the standard deviation of the helix height sets (see Table 3.1). (b) Maximum optical activity as a function of helix height for data from the calculations using the COMSOL model. In both (a) and (b) we recognize a trend in which short helices have smaller maximum optical activities than tall helices.

We investigate the trend of $(O.A.)_{\max}$ as a function of helix height. In Figure 3.7 and 4.4, these trends are displayed for the experimental and calculated data and in order to compare these results, we show these graphs together in Figure 5.1. Figure 5.1a shows the maximum optical activity as a function of helix height for the experimental data and Figure 5.1b for the calculated data. As expected, we observe that the actual values of the maximum optical activity differ due to some parameter differences. While the maximum optical activity ranges from ~ -0.45 to ~ -0.65 in the calculated data, it ranges from ~ -0.15 to ~ -0.45 in the experimental data. But the trends in both graphs show good qualitative agreement: short helices have a smaller maximum optical activity than tall helices.

An explanation for the difference in the experimental and calculated data could be that the gold layer on the fabricated helices is inhomogeneous, as discussed in Section 2.1.6. The COMSOL model assumes that the gold layer is perfectly homogeneous on all sides of the helix. We expect that the inhomogeneity of the gold layer on the

fabricated helices leads to scattering events. This scattering may result in a change of polarization. When the polarization becomes less circular, we expect this to lead to a decrease of absorption which translates to maximum optical activity that is less negative.

As mentioned in Chapter 4, the lattice constant of the array is 400 nm in the experiment and 600 nm in the calculated data. Thus, the density of the array is higher in the experiment than in the calculation. The work of Gansel et al. [16], on micrometer sized pure gold helices, shows a more pronounced transmission dip when either the lattice constant is decreased (while the major radius is kept constant) or when the major radius is increased (while the lattice constant is kept constant). This translates to a large maximum optical activity for high densities in contrary to the results we find when comparing the high density in the experiment with the lower density in the calculation. However, this difference is only in the order of a factor two and we assign this difference to the inhomogeneous gold layer in the experiment as mentioned earlier.

Additionally, we can compare the trend displayed in Figure 5.1 with the theoretical work of Gansel [16]. In their work, the transmission of LCP and RCP was studied for helices with different heights of micrometer sizes. The dip in transmission for LCP increased when increasing the helix height while the transmission of RCP was constant. This would correspond to an increase in maximum optical activity. In agreement with their findings, we also observe that the maximum optical activity becomes larger for taller helices.

5.2 Outlook

We have measured large optical activity on the array of plasmonic nanohelices. Nevertheless, there are many parameters to be investigated in order to understand the light-matter interaction in the complex structures studied in this work. The results of the experiment described in this thesis are qualitatively confirmed by calculations using model made in COMSOL Multiphysics. The fabrication method to make nanohelices is well understood and can be used to fabricate nanohelix arrays with varying parameters. Thus in the future, using this unique fabrication method followed by transmission measurements, we can investigate how helix parameters like gold layer thickness and array density influence the optical activity.

First, we would like to further investigate what influence the lattice constant has on the optical activity. From previous research by Gansel [16], we expect that a higher density of helices would result in a larger maximum optical activity. Making arrays of higher density is accomplishable using our method by changing this parameter in the streamfile, though this approach is limited. The increase in density will eventually cause the single helices to merge into one big structure and the chiral effects will

likely disappear or at least change compared to single helices. Where this limit is would have to be studied empirically. Up till now a lattice constant of 300 nm has been successfully fabricated for helices with a major radius of ~ 80 nm. After sputtercoating a layer or 40 nm of gold, the helices did not touch yet.

Another parameter that we can vary is the thickness of the gold layer on the nano-helices. Calculations showed that the absorption of LCP compared to RCP is significantly larger in the gold shell of the helix than in the gold between the helices on the substrate, even though these two layers have the same thickness. This absorption ratio was determined by comparing absorption coefficients calculated in the model using

$$\text{absorption ratio} = \frac{A_{\text{LCP, helix (substrate)}}}{A_{\text{RCP, helix (substrate)}}} \quad (5.1)$$

where $A_{\text{LCP, helix (substrate)}}$ is the absorption coefficient of either the gold on the helix or the gold on the substrate when illuminated with LCP. In Figure 5.2 this absorption ratio is displayed as a function of wavelength. In this graph it can be seen that the absorption in the substrate is nearly the same for both LCP and RCP since the ratio is around 1. But around $\lambda = 700$ nm, the absorption of LCP in the gold layer on the helix is about 20 times higher than the absorption of RCP. A high absorption corresponds to a low transmission of LCP at these wavelengths and combined with a constant transmission of RCP leads to the optical activity measured in this work. Assuming that the thickness of the layer has influence on the absorption, changing the gold layer thickness on the helices is likely to influence the optical activity.

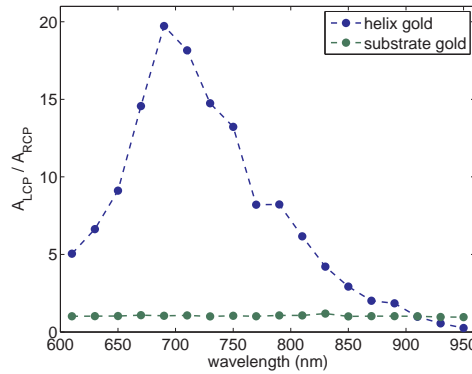


Figure 5.2: Absorption ratio $A_{\text{LCP}}/A_{\text{RCP}}$ of absorption of LCP compared to RCP as a function of wavelength derived with the COMSOL model. Calculation was performed on an array of left-handed helices with a lattice constant of 800 nm. The helix in the model had a height of 850 nm, a major radius of 90 nm and the gold layer on helix and substrate was 20 nm. The blue curve represents the absorption ratio $A_{\text{LCP}}/A_{\text{RCP}}$ of the gold on the helix. The green curve represents the absorption ratio in the gold on the substrate, between the helices. Around $\lambda=700$ nm, the absorption in the helix gold is about ~ 20 times higher than the absorption in substrate gold even though the thicknesses are the same.

A thicker layer of gold can be sputtered on the helices. We should pay attention to how a thicker gold layer influences the helix geometry. At some point the well defined geometry might get hidden under the thick gold layer. Furthermore, the sputtering also reaches the substrate and when does the gold get too thick, most of the incident light will already be absorbed in the layer on the substrate between the helices, since the light first has to travel through this layer for the transmission measurement.

When comparing nanohelix arrays with different gold layers, all other helix parameters should be constant and due to the many (subtle) factors that influence our deposition method this is a tough achievement. A possible solution to measure the effect of gold layer thickness, is to sputter on one and the same array nanohelices in steps and performing the transmission measurements in between. For instance, first a layer of 20 nm can be sputtered onto an array followed by a transmission measurement. Next, a second layer of 20 nm can be sputtered on the already sputtered array which results in a gold layer on the array with a total thickness of 40 nm. Again, a transmission measurement can be performed and transmission of the two layer thicknesses can be compared. A transmission measurement can be done relatively fast so hopefully, no contamination or oxidation occurs between different sputtering events. A confirmation that this works for two different thicknesses was tested. First, we measured on an array with a thin layer of gold sputtercoated on it. When we did not detect significant optical activity, we added an extra layer by a second sputtercoating event. In a second transmission measurement we did measure significant optical activity. This indicates that multiple sputtercoating events are possible without significant change in the geometry.

In the future, applications using plasmonic nanohelices will require arrays of identical helices, in order to obtain perfect tunability. First, a manner to fabricate arrays with identical helices, is to make the arrays smaller by decreasing the number of helices. When making a smaller array, the differences in helix parameters will be smaller since the time between the deposition of the first and last array is short. From the experiment we have learned that good results are achieved when using a spot with FWHM of 3 μm , so an array of 3.5 $\mu\text{m} \times 3.5 \mu\text{m}$ should be sufficient.

Another possible way to fabricate arrays with identical helices is to use scripts to transfer the pattern to the microscope, instead of streamfiles. Using a script, the stage with the sample can be moved during deposition and this could possibly decrease the difference in height when the sample is moved in such a way that the deposition is always at the same distance to the GIS. We investigated this option, but the movements of the stage were too coarse in the deposition of nanometer-sized helices. However, we need to test if using a script in between several (small) arrays results in arrays with identical helices, since the arrays are deposited at an equal distance to the GIS.

Besides moving the stage, one also could possibly compensate for height differences due to the GIS location by changing the dwell time. Basically, dwell times should be long far away from the GIS and short close to the GIS. The change in dwell time should be quite subtle and it should be investigated in detail in what way the dwell time has to vary to compensate for height differences due to the GIS location.

A final element of our fabrication method that can be improved is the method used for coating the helices with gold. The sputtering turns out to cover the helices in a sufficient way to measure optical activity, but the gold layer on the helices is not perfectly homogeneous. Sputtercoating also causes the formation of a gold layer on the substrate between the helices which absorbs a lot of light before the light reaches the helices. From calculations we know that the gold in the substrate shows not difference in absorbance for LCP and RCP (see Figure 5.2) and therefore does not contribute to the optical activity. In the future a way to ensure homogeneity and not form a gold layer on the substrate would be to use the method of electrochemical deposition. The surface of ITO is chemically functionalized in a different way than the deposited SiO_x . By seeding gold nanoparticles only on the SiO_x , which would not be able to stick to the ITO, a uniform gold layer could be deposited *only* on the helices. This would make it possible to study different gold layer thicknesses on the helices in detail and additionally measure on thicker gold layers since absorption in the substrate layer would no longer occur.

6 Acknowledgements

Wow, as the final part of my master thesis, I am writing my acknowledgements. This year at AMOLF has been a truly great one. The environment at AMOLF is fantastic. The support staff is unique and gives everybody the possibility to do great work.

Kobus, thank you so much for letting me work in your group this year. I have learned a lot and done challenging and fun research. I experienced a little bit of all aspects of research at AMOLF: fabrication, lab work and calculations. Your ‘Kobus teaching moments’ are always good and the analogies you sometimes use for difficult physics things are brilliant. And, as a great ending of a great year, you’re letting me join to Utah this summer to give a talk at the NFO conference, which is an experience I am really looking forward to.

Anouk, you were an excellent supervisor. You were a great mental support, always ready to listen to my frustrations and always putting them into perspective for me. From the beginning on you gave me confidence and let me work very freely. And of course, we simply had a nice time, us girls in the NanoOptics group.

Nir, thanks for teaching me a lot. Your critical view on things made me do better in all kinds of ways. Especially when preparing the colloquium you said the things I needed to hear to give a better talk.

Aron, you were my big support in my (short) lab career. You taught me a lot in those couple of weeks about lasers and data analyzing in Matlab. Thanks for that.

Ruben, Boris and Matthias, thanks for the nice time in the group and the discussions on my research.

Hinco, you’re a great technician. Due to my short time in the lab we didn’t work together that much, but you made me a great sample holder. I have the feeling you’re always in a good mood and that’s why it’s nice to be around you.

To all the people of the Center for Nanophotonics, thank you for the nice colloquia, poster sessions and coffee breaks.

Hans, Dimitry and Andries, thanks for all your help in the SEM room and the clean-room. Especially Hans, thanks for teaching me everything there is to know about electron microscopy.

Quirien, Paulus, Nienke and Martha, thanks for showing such an interest in my work and always asking questions about what exactly I was doing. I remember realizing, during a conversation at the kitchen table at the beginning of the year, that a helix has the same twist as seen from the bottom and the top.

Last but not least, I would like to thank Jelle. You’ve been and are my ‘steun en toeverlaat’.

Dolfine Kusters, July 10, 2014.

Appendix A Structure of a streamfile

From a streamfile, the system can derive what coordinates the electron beam should scan and how long it should remain at each coordinate, a parameter called dwell time. Three main columns form the streamfile: the dwell time (in multiples of 100 ns), the x-coordinate and the y-coordinate. The x-coordinate and y-coordinate together represent one pixel in the field of view. In this setup, the writing field is divided in $2^{16} = 65536$ pixels in the x- and y-direction. The top left pixel has coordinates (0, 0) and the bottom right pixel has coordinates (65536, 65536). This has the consequence that magnification has influence on the deposition. Depending on the magnification that the system has when running a streamfile, the pixelsize is determined. A larger magnification leads to a smaller horizontal field width (HFW), which corresponds to a smaller pixelsize. Furthermore, the streamfile contains a header. In this header, the number of loops and the total amount of coordinates is given. In Table A.1 an example of the beginning of such a streamfile is shown. The 16 bit system leading to the 2^{16} pixels is represented by s16, the 1 on the second line stands for that this streamfile is looped once, there are 207911 coordinates in the streamfile and the dwell time is 14 ms.

s16		
1		
270911		
140000	33321	33242
140000	33320	33248
140000	33320	33254
...

Table A.1: Example of the top of a streamfile containing 207911 coordinates of which 3 are displayed. The left column first gives the header. s16 stands for the 16-bit system that is available and 1 is the number of loops followed by the number of coordinates 207911. After the header, the left column contains the dwell time, in this case 14 ms (multiple of 100 ns) the column in the middle contains the x-coordinates and the right most column contains the y-coordinates. Then the electron beam starts at pixel (33321,33242), stays there for 14 ms, and then moves to pixel (33320,33248).

References

- [1] E. Hendry, T. Carpy, J. Johnston, M. Popland, R. V. Mikhaylovskiy, a. J. Laphorn, S. M. Kelly, L. D. Barron, N. Gadegaard, and M. Kadodwala, *Ultra-sensitive detection and characterization of biomolecules using superchiral fields.*, Nature nanotechnology **vol. 5**, no. 11, pp. 783–7 (2010)
- [2] M. van Lare, F. Lenzmann, M. Verschuuren, and A. Polman, *Mode coupling by plasmonic surface scatterers in thin-film silicon solar cells*, Appl. Phys. Lett. **vol. 101**, no. 22, pp. 221110 1–4 (2012)
- [3] P. Spinelli and A. Polman, *Light Trapping in Thin Crystalline Si Solar Cells Using Surface Mie Scatterers*, IEEE Journal of Photovoltaics **vol. 4**, no. 2, pp. 554–559 (2013)
- [4] A. Polman, *Plasmonics Applied*, Science **vol. 322**, no. November, pp. 868–869 (2008)
- [5] M. I. Stockman, *Nanoplasmonics: The physics behind the applications*, Physics Today **vol. 64**, no. 2, p. 39 (2011)
- [6] T. W. Ebbesen, H. J. Lezec, H. Ghaemi, T. Thio, and P. Wolff, *Extraordinary optical transmission through subwavelength hole arrays.*, Nature **vol. 391**, pp. 667–669 (1998)
- [7] A. Guijarro and M. Yus, *The Origin of Chirality in the Molecules of Life*, The Royal Society of Chemistry (2009)
- [8] I. Agranat, H. Caner, and J. Caldwell, *Putting chirality to work: the strategy of chiral switches.*, Nature reviews. Drug discovery **vol. 1**, no. 10, pp. 753–68 (2002)
- [9] A. Yariv and P. Yeh, *Optical Waves in Crystals: Propagation and Control of Laser Radiation*, John Wiley and Sons, Inc (1984)
- [10] Z. Fan and A. O. Govorov, *Plasmonic circular dichroism of chiral metal nanoparticle assemblies.*, Nano letters **vol. 10**, pp. 2580–2587 (2010)
- [11] B. M. Maoz, R. van der Weegen, Z. Fan, A. O. Govorov, G. Ellestad, N. Berova, E. W. Meijer, and G. Markovich, *Plasmonic chiroptical response of silver nanoparticles interacting with chiral supramolecular assemblies.*, Journal of the American Chemical Society **vol. 134**, pp. 17807–13 (2012)
- [12] M. Hentschel, T. Weiss, S. Bagheri, and H. Giessen, *Babinet to the half: coupling of solid and inverse plasmonic structures.*, Nano letters **vol. 13**, no. 9, pp. 4428–33 (2013)

-
- [13] R. Schreiber, N. Luong, Z. Fan, A. Kuzyk, P. C. Nickels, T. Zhang, D. M. Smith, B. Yurke, W. Kuang, A. O. Govorov, and T. Liedl, *Chiral plasmonic DNA nanostructures with switchable circular dichroism.*, Nature communications **vol. 4**, p. 2948 (2013)
- [14] M. Schäferling, D. Dregely, M. Hentschel, and H. Giessen, *Tailoring Enhanced Optical Chirality: Design Principles for Chiral Plasmonic Nanostructures*, Physical Review X **vol. 2**, p. 031010 (2012)
- [15] J. K. Gansel, M. Thiel, M. S. Rill, M. Decker, K. Bade, V. Saile, G. von Freymann, S. Linden, and M. Wegener, *Gold helix photonic metamaterial as broadband circular polarizer.*, Science (New York, N.Y.) **vol. 325**, no. 5947, pp. 1513–1515 (2009)
- [16] J. K. Gansel, M. Wegener, S. Burger, and S. Linden, *Gold helix photonic metamaterials: a numerical parameter study.*, Optics express **vol. 18**, pp. 1059–69 (2010)
- [17] J. G. Gibbs, a. G. Mark, S. Eslami, and P. Fischer, *Plasmonic nanohelix metamaterials with tailorable giant circular dichroism*, Applied Physics Letters **vol. 103**, no. 21, p. 213101 (2013)
- [18] R. Stewart, *Insulating Films Formed Under Electron and Ion Bombardment*, Physical Review **vol. 45**, p. 488 (1934)
- [19] R. W. Christy, *Formation of Thin Polymer Films by Electron Bombardment*, Journal of Applied Physics **vol. 31**, no. 9, p. 1680 (1960)
- [20] W. F. van Dorp, C. W. Hagen, P. a. Crozier, and P. Kruit, *Growth behavior near the ultimate resolution of nanometer-scale focused electron beam-induced deposition.*, Nanotechnology **vol. 19** (2008)
- [21] S. J. Randolph, J. D. Fowlkes, and P. D. Rack, *Focused, Nanoscale Electron-Beam-Induced Deposition and Etching*, Critical Reviews in Solid State and Materials Sciences **vol. 31**, no. 3, pp. 55–89 (2006)
- [22] L. Reimer, *Scanning Electron Microscopy*, Springer - Verlag Berlin (1998)
- [23] FEI Company, www.fei.com, 5350 NE Dawson Creek Drive, Hillsboro, OR, *Application Note - The Gas Injector System for the SEM and DualBeam* (2006)
- [24] *COMSOL webpage*, <http://www.comsol.nl/comsol-multiphysics>
- [25] P. B. Johnson and R. W. Christy, *Optical constants of the noble metals*, Phys. Rev. B **vol. 6**, pp. 4370–4379 (1972)